TECHNICAL PAPER

A damage index proposal for shear-after-impact of laminated composite plates

Gabriel Sales Candido Souza[1] · **Marcelo Leite Ribeiro**[1] · **Volnei Tita**[1,2]

Abstract

This work presents a damage index proposal based on an experimental approach to evaluate the behavior of laminated fiber-reinforced composite plates under in-plane shear-after-impact conditions. Therefore, drop-weight experimental tests for low-energy impact (face-on in the barely visible impact damage range) are performed in laminates, as well as in-plane shear tests are carried out by 3-rail device to obtain stress–strain curves for pristine and impact-damaged composite plates. A new coupon based on the ASTM standards is designed to fit impact and in-plane shear experimental devices. The phenomenological damage index for shear-after-impact is energy-based being able to quantify the damage severity in the composite plates as shown by experimental results. Simple guidelines for its determination are also summarized. Furthermore, computational simulations via ABAQUS with a User Material (UMAT) subroutine accounting for progressive damage analysis are performed to predict damage index values for different degradation scenarios. Finally, it is discussed and concluded that the proposed damage index and the experimental approach can be combined with the already consolidated procedures, such as flexure- and compression-after-impact, to evaluate with more accuracy the residual strength of impacted laminates of fiber-reinforced composite materials.

Keywords Damage index · Laminated composites · Low-energy impact · Post-impact behavior · Shear-after-impact · Progressive damage analysis

1 Introduction

Composite materials play an important and increasing role in the aeronautical, automobile, and energy industries due to the necessity of designing extremely light structures owning high specific strength and stiffness since these designs

✉ Gabriel Sales Candido Souza
gabrielsales@usp.br

Marcelo Leite Ribeiro
malribei@usp.br

Volnei Tita
voltita@sc.usp.br

1 São Carlos School of Engineering, Aeronautical Engineering Department, University of São Paulo, Av. João Dagnone, São Carlos, SP 13563-120, Brazil

2 Faculty of Engineering, Mechanical Engineering Department, University of Porto, Rua Dr Roberto Frias, 4200-465 Porto, Portugal

are commonly very weight-sensitive [1, 2]. Although composites, especially the fiber-reinforced polymer (FRP) kind, meet different applications in which these are very cost-effective and bring many advantages over their metallic counterparts, there are still challenges involving their employment [2]. For example, failure and its mechanisms are complex and not fully understood yet [3, 4], and laminated composite structures do not possess high transverse strength, being susceptible to severe damage that can arise from impact events [5]. Nevertheless, composite materials can offer improvements in the crashworthiness performance of structures, usually, tube-like ones, used for example in motorsports [6] when designed to absorb, in a controlled manner, the impact energy in the axial direction [7]. Commonly this is not the case for aircraft structures, where impact damage can occur from numerous situations such as tool dropping during manufacture, maintenance, and assembly procedures, flying debris from take-off and landing, collision with another vehicle, and bird strike, among others. For example, foam-composite sandwich panels (e.g., FRP skins with a foam core material) are widely used in

the aerospace industry as an impact absorber material under high-velocity impact (HVI) events [8] that relate to collision or bird strike examples. The first example related to tool dropping is representative of low-energy impact (LEI) [5, 9–11], which usually causes minimal superficial damage in laminated composites, while the internal structure can exhibit a variety of complex intralaminar and interlaminar damage mechanisms. This type of damage is commonly classified as barely visible impact damage (BVID), which can highly influence the laminate residual strength and remain undetectable during scheduled inspection and maintenance procedures [9–11]. Therefore, due to the challenges in the prediction of failure, residual strength, and life during the operational service of composite materials, these still found some limitations in their application in the aeronautical industry. Since aeronautical certification agencies (e.g., FAA—Federal Aviation Administration) must guarantee security and airworthiness, this usually implies on structures designed considering infinite life philosophy, then the structure does not suffer fatigue when considering its loading envelopes resulting in a conservative design approach [12]. Also, the LEI behavior is highly dependent on specimen and impactor masses and geometries, impact energy and force, boundary conditions, layup, and stiffness [13].

Considering the aspects pointed out, the study of damage tolerance design applied in composite structures has gained increasing attention over the years to overcome over-dimensioning practices. In a nutshell, it is necessary to demonstrate that such structures are capable to possess residual strength even with impact damage and, depending on the application, to show that does not have excessive deformations. This condition must be true until the detection of the damage, and after its identification, the structure must be repaired, either portions of the structure or even the whole part must be replaced. Thus, one of the most worrying categories of impact-induced damage is the BVID because it is very penalizing and may be difficult to detect [11]. Additionally, the prediction of damage extension, severity, and progression are extremely important. Understanding and applying these concepts lead to the less-conservative design philosophy of damage tolerance, which represents a great leap in the context of sustainable development. Thus, many researchers dedicated studies proposing methodologies to evaluate the post-impact behavior of laminated composite structures under various types of loadings using the compression-after-impact (CAI) approach, which is the most explored one. Several studies can be found on the topic, and there is agreement that the most affected property of laminates subjected to LEI is the compressive strength due to buckling [5, 9–11]. Also, there is the flexure-after-impact (FAI) approach to evaluate this post-impact behavior of laminates which in some sense tries to mimic the CAI technique inducing compression load in one portion of the structure under 3- or 4-point bending

tests [14, 15]. Besides, to know if the structure still possesses the strength to withstand post-impact loads, and if it is necessary to repair it, damage indexes (DIs) have been proposed to quantify these. Furthermore, there are only a few works considering the shear-after-impact (SAI) behavior assessment [16, 17] of composite structures under LEI and BVID conditions, which can be counter-intuitive since these are commonly found under combined stress states.

In the presented context, this work arises due to the lack of studies in the field aiming to investigate the post-impact behavior of composite laminates under in-plane shear loading. Thus, based on the previous researches for FAI conducted by Medeiros et al. [14, 15], an experimental analysis procedure is proposed for SAI where LEI is done in a drop-tower apparatus, and further shear testing is carried out using the 3-rail test device, both standardized by the ASTM D7136 [18] and D4255 [19], respectively. These tests are set for a usual $[0°]_{16}$ unidirectional carbon fiber-reinforced polymer (CFRP) laminate so that the major damage/failure mechanisms seen during them are intralaminar ones in the polymer matrix. To fit both test layouts, a new geometry for the coupons is designed especially for SAI testing. Based on the results from rail and impact tests, an energy-based damage index for SAI is proposed. Then, finite element analyses (FEA) are carried out to computationally obtain values for the damage index considering other impact-induced damage situations. For these, a previously developed continuum damage mechanics (CDM) material model accounting for progressive damage is employed, being implemented as a user material subroutine (UMAT) linked to ABAQUS finite element package. In the end, it is discussed that the proposed analysis procedure and the damage index for SAI can be used as complementary to the CAI and FAI approaches.

2 Damage index proposal

2.1 Proposed procedure for SAI analysis

Inspired by the works developed by Medeiros et al. [14, 15] for FAI, here is proposed an experimental energy-based approach to quantify a damage index for in-plane SAI. As depicted in Fig. 1, rail tests are carried out for undamaged and damaged coupons. First, a shear stress–strain curve is obtained for an undamaged coupon. After that, two drop-weight tests (low-energy impact—LEI) are done to introduce damages in another coupon at different positions and faces (top and bottom). Then, the resulting shear stress–strain curve for the undamaged coupon is used as a basis for comparison with the results obtained by performing a rail test on the damaged one. It is important to notice that a new coupon geometry is proposed for the present SAI analysis.

Fig. 1 Overview of the proposed procedure for in-plane shear-after-impact (SAI) analysis
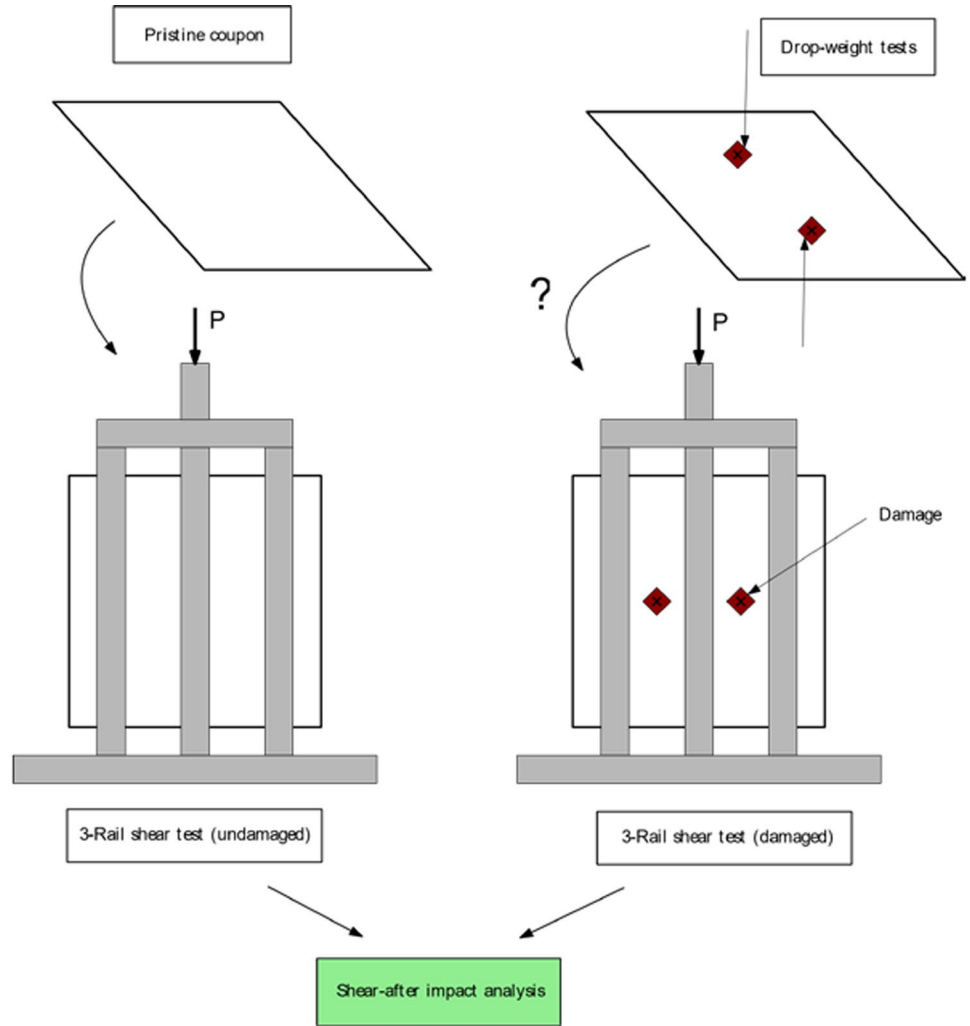
In the proposed procedure, there is an important condition related to the drop-weight tests, which must be low-energy ones. Thus, before carrying out the rail tests on the damaged coupons, it must be guaranteed that the impact damage is within the barely visible range. For this, the loss-factor theory proposed by Christoforou and Yigit [20–24] is employed in which a dimensionless parameter ζ_w called by loss-factor is defined in Eq. (1) and used to analytically characterize the behavior of an impact event.

$$\zeta_w = \frac{1}{16}\sqrt{\frac{K_\alpha M_i}{I_1 D^*}} \tag{1}$$

where K_α is the contact stiffness, M_i is the impactor mass, I_1 is an inertial parameter, and D^* is the laminate effective bending stiffness. Accordingly, these parameters are given as follows:

$$K_\alpha = 10.4 R_i S^L \tag{2a}$$

$$I_1 = \frac{M_P}{ab} \tag{2b}$$

$$D^* = \frac{1}{2}\left(D_{12} + 2D_{66} + \sqrt{D_{11}D_{22}}\right) \tag{2c}$$

where M_P, a, and b are the mass, length, and width of the plate, respectively, R_i is the impactor radius, S^L is the material in-plane shear strength, and D_{ij} are the components of the bending-torsion stiffness matrix from the classical lamination theory (CLT) for $i = 1, 2$ and 6, written in the global coordinate system [2]. Following, the condition that needs to be satisfied for the characterization of LEI through the loss-factor is given by:

$$\zeta_w \geq \sqrt{\frac{0.68}{\lambda}} \tag{3}$$

with λ defined as relative stiffness and being the parameter that governs the normalized impact response, which is obtained as follows:

$$\lambda = \frac{K_{bs}}{K_\alpha} \tag{4}$$

where the plate bending-shear stiffness K_{bs} is calculated as:

$$K_{bs} = \frac{D^*}{0.0116a^2} \tag{5}$$

Equations (4) and (5) are only valid for Olsson's [25] definition of large mass impact (i.e., $M_i \geq 2M_P$). In addition, in the present work, it was preserved the original notations used by Christoforou and Yigit [20–24].

In Fig. 2, there are more details about the proposed approach for the shear-after-impact analysis with the verification of the condition for LEI. After manufacturing the coupons, a rail test of the pristine one is carried out. Then, the obtained results are compared to those from tensile tests in $[\pm45°]_{ns}$ angle-ply laminates. Thus, the shear stress–strain curves from both tests are suitably compared, and if there is a good agreement between the results, then the rail test is considered "acceptable." In other words, the manufacturing procedure and testing fixture can be considered "validate." In parallel, two identical impact tests on different sides of

the same coupon are performed as shown in Fig. 1. However, the condition imposed by Eq. (3) must be preserved to have a coupon with two impact damages to be evaluated in the 3-rail shear test as shown in Fig. 1 and Fig. 2. In the end, the SAI stress–strain curves for damaged and undamaged coupons are used to calculate the damage index.

Figure 3 shows the equipment used in the low-energy impact and shear tests. For the LEI tests, the coupon is fixed by four toggle clamps attached to an inertial base (5) of the drop-tower (Fig. 3a). A support frame (1) is guided by two parallel beams. This support is used not only to hold the hemispherical impactor with a Kistler 9011A load cell (LC—3), but also to set the test height. This load cell is a piezoelectric transducer with the capability of compression forces measurement at the z-axis (i.e., the same direction of gravitational acceleration) under dynamic and quasi-static load conditions. Quartz crystals generate an electric charge proportional to the mechanic load with a sensitivity of 4.3 pC/N and 96 kN range. The displacement measurement is done by a laser distance sensor (LDS—2) model M70LL/50 from MEL Intelligent Sensor & Measuring Systems, which quantifies the relative distance between the impactor's tip and a T-beam (painted white for the LDS well-function) attached to the support frame as shown in detail in Fig. 3b. It has a measuring range of 50 mm, a sampling rate of 400 kHz,

Fig. 2 SAI analysis flowchart: Evaluation of the manufacturing procedure, testing fixture and impact conditions for LEI
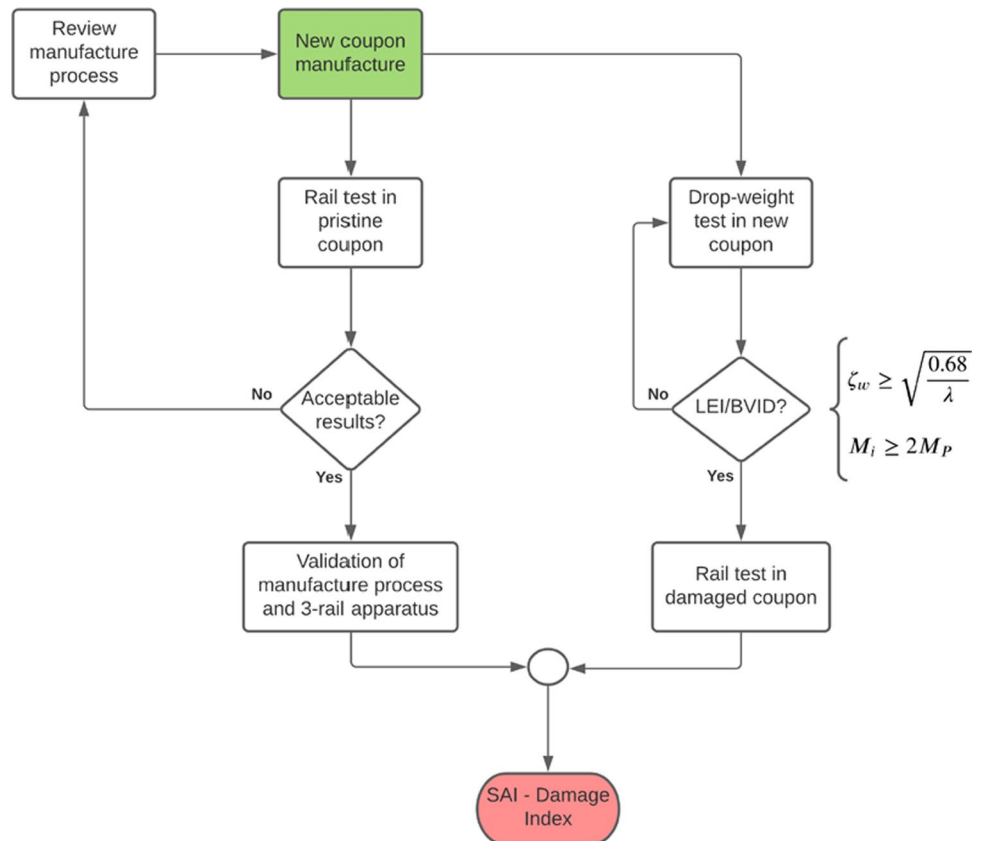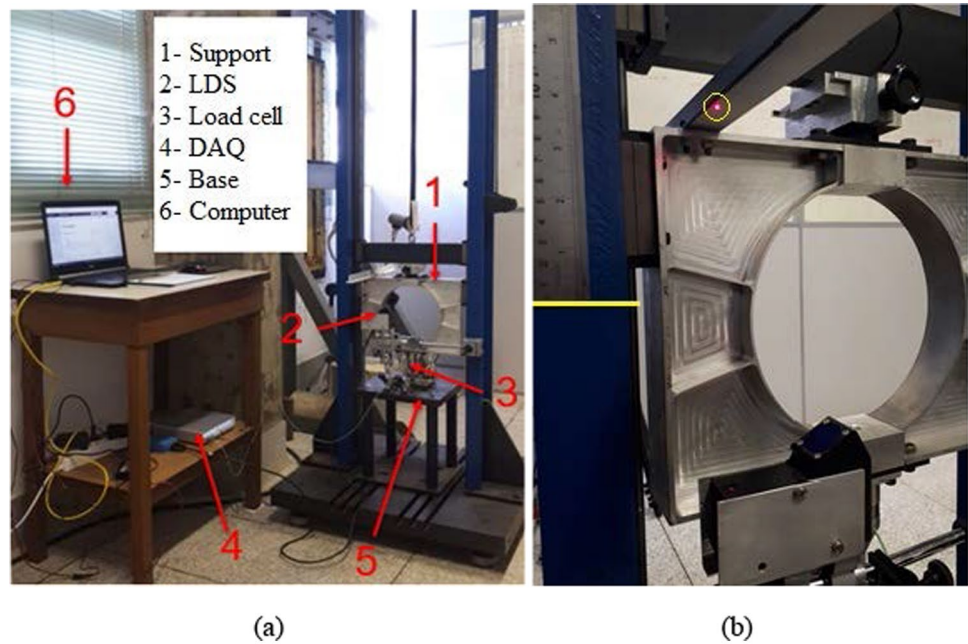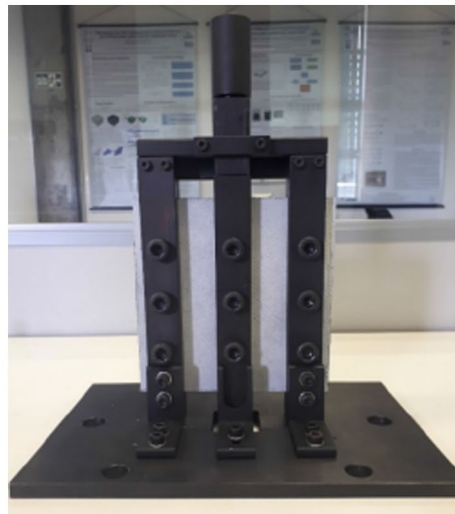
Fig. 3 Drop-tower complete system **a**; distance measurement scheme (the laser sensor in details) **b**; 3-rail test apparatus **c**

(a)

(b)

(c)

and 100 kHz of measuring frequency being capable to capture displacements that occur during an impact event with high accuracy. Both load and displacement signals are recorded by the charge amplifier/data acquisition unit (DAQ—4) LabAmp 5165A from Kistler and sent to a personal computer (6) to be posteriorly analyzed. The DAQ has the capability to capture up to 200 kSps (kilo samples per second) in each of its four channels simultaneously, and it also enables the user to see real-time results.

For displacement characterization, since the physical quantity captured is voltage, distance conversion has to be done with aid of the LDS calibration curve. Considering the relative distance of the beam and impactor heights, the conversion is given as,

$$u_i(t) = -2.5\big(V_i(t) - V_0\big) \qquad (6)$$

where u_i is the displacement in millimeters, $V_i(t)$ is the measured voltage over time of the i-th data point, and V_0 is the reference voltage measured as the impactor-target contact (both in volts). The minus sign on the right hand-side of Eq. (6) is introduced to make the displacement positive.

The pristine and damaged impact coupons are submitted to the in-plane shear test using the 3-rail apparatus shown in Fig. 3c. This kind of shear device was selected because the coupon geometry can be easily redesigned to fit impact and shear tests. As can be observed, coupons are attached to the rails by screws. The side rails (on the left and the right side) are fixed in the base, while the center rail is free to

move in the vertical direction (Fig. 3c). Thus, a universal machine head can apply the load on the top of the central rail, which can move upward or downward. In the present work, the central rail is moved downwards (Fig. 1) by using an INSTRON® 5900 universal testing machine that has a 250 kN load cell capacity, then the regions of the coupon between the side rails and central rail are loaded under in-plane shear. These portions of the coupons consist of the region of interest (ROI), where the shear strain fields are obtained via the digital image correlation (DIC) technique where a series of photographs of the ROIs are taken by a digital camera (in this study, a CANON EOS 350 with an acquisition rate of 0.17 images/second) that is connected to a computer. Then, later, the images taken in a test are treated using the GOM Correlate software.

2.2 Damage index for SAI

To determine the residual strength of the structure after an impact event, it is possible to quantify this value via an indirect approach by defining a damage index. Thus, this index can assess the damage severity, providing the necessity of performing or not a repair of the damaged impact structure when the damage index calculation is integrated into a structural health monitoring (SHM) system. Since the SAI analysis is a straightforward procedure based on the comparison of the shear stress–strain curves of both pristine and damaged impact laminates, the strategy adopted to define a damage index is energy-based, following Eq. (7).

$$\text{DI}_{\text{SAI}} = 1 - \frac{\overline{E}_D}{\overline{E}_P} \tag{7}$$

in which $\overline{E}_D = E_D - E_D^{\min}$, $\overline{E}_P = E_P - E_D^{\min}$. Also, E_D and E_P are the reference energy density values associated to the damaged and pristine laminates, respectively. Notice that from Eq. (7), the damage index ranges from "0" (no damage) to "1" (fully damaged) with the parameters $\overline{E}_D$ and $\overline{E}_P$ defined such as this is always true. Moreover, the parameter $E_D^{\min}$ is the minimum allowable energy for a damaged laminate, which is related to the ultimate in-plane shear stress of the pristine laminate, given by:

$$E_D^{\min} = \int_0^{\gamma_{12}\text{frac}} \frac{\tau_{12}^{\text{ult}}}{\text{FS}} \mathrm{d}\gamma \tag{8}$$

where $\gamma_{12}^{\text{frac}}$ is the fracture shear strain, τ_{12}^{ult} is the ultimate in-plane shear stress of the undamaged coupon, and *FS* is the factor of safety, commonly adopted as equal to 1.5 for aeronautic structures, considering the flight envelope. Thus, a laminate subjected to a LEI, providing an energy value greater than that one defined in Eq. (8), will show a damage index value for in-plane shear within the range

$0 \le \text{DI}_{\text{SAI}} \le 1$, since $E_D^{\min} \le E_D \le E_P$. Thus, if $E_D = E_D^{\min}$, then $\text{DI}_{\text{SAI}} = 1$, and if $E_D = E_P$, then $\text{DI}_{\text{SAI}} = 0$.

3 Application of the proposed procedure

3.1 Specimen preparation

An epoxy pre-impregnated (prepreg) UD carbon fiber system from Texiglass Industry and Textile Commerce (areal weight 208 g/m^2 and 0.29 mm thickness) is used for manufacturing the specimens. The composite laminates are produced by hand-layup technique with a vacuum bag inside a temperature-controlled oven (Fig. 4a) following a sequence of systematic proceedings to guarantee the reliability and reproducibility of laminates and results.

The adopted lamination sequence detailed in Fig. 4b is as follows: (i) thick glass plate (not shown) used as a mold for the laminates preventing warping during cure; (ii) Teflon film (A) used to release the plate easier; (iii) prepreg carbon plies; (iv) perforated film (B) to control the resin flux during cure; (v) peel-ply film (C) for resin excess absorption; (vi) pressure redistribution mesh (F) for vacuum homogenization inside the bag; (vii) breather cloth layer (E) to conduct volatile and trapped air components from the bag to the vacuum pump connector; (viii) metallic plate (not shown) to aid laminate molding; (ix) vacuum bagging film (not shown) with sealant tape; and (*x*) vacuum connector (*F*). This sequence is adopted for the standardization of the composite plates, making possible a consistent study in a comparative manner. Also, for all laminates, the same cure cycle (Fig. 4c) is employed for the same reason described above.

Measurements of fiber V_f and matrix V_m volume fractions are done following the procedure B of the ASTM D3529 standard [26], as depicted in Table 1.

To obtain the mechanical properties and strength values of the composite material shown in Table 2, a test campaign is carried out following the adequate standards [27, 28] for $[0°]_8$, $[90°]_8$, and $[\pm45°]_{4s}$ specimens. It is important to highlight that to measure strain fields during the tests, it used DIC technique as well.

Regarding the drop-weight and rail tests, adaptations of the standardized specimens are required. On the one hand, ASTM D7136 standard [18] specifies a rectangular coupon (100×150 mm) fixed by four toggle clamps (Fig. 5a) in an inertial base, which contains three guiding pins to constrain movement in the plane (Fig. 5a). On the other hand, ASTM D4255 standard [19] specifies a rectangular coupon (140×160 mm) drilled with nine holes with 10~13 mm of diameter. Thus, a new coupon geometry that suits both

Fig. 4 Oven used for cure **a**; adopted lamination sequence with required materials **b** and; example of expected *vs.* experimentally obtained cure cycle **c**
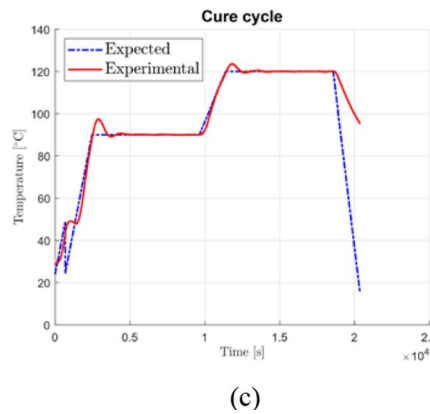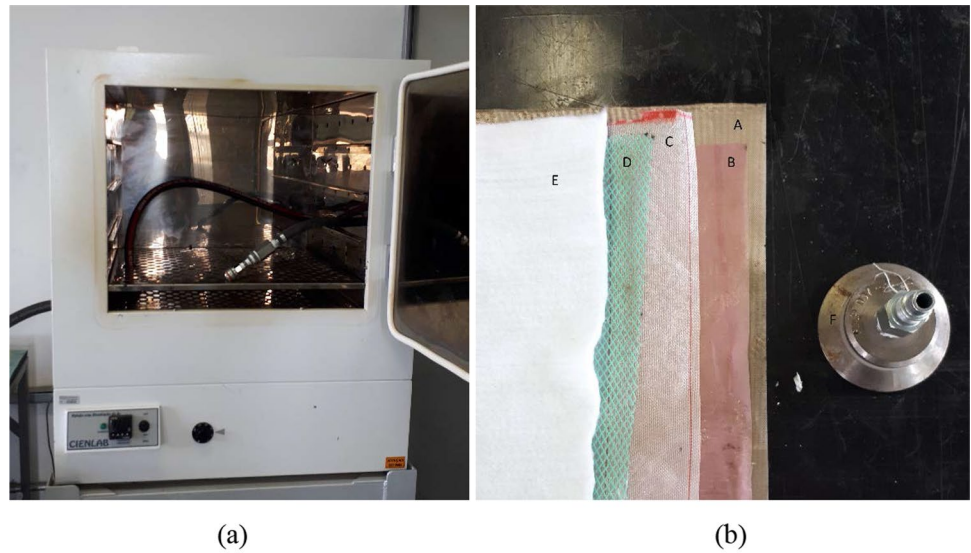

(a)

(b)

(c)

Table 1 Material data

Property	Unit	Value	Procedure
Mean matrix volume fraction	n/a	0.359	ASTM D3529
Mean fiber volume fraction		0.641	
Reinforcement density	g/cc	1.9	Manufacturer data
Matrix density		1.3	

Table 2 Mechanical properties and strength values

Elastic properties		Strength values	
E_{11}[GPa]	122.33	X_T[MPa]	1404.08
E_{22}[GPa]	6.78	Y_T[MPa]	21.55
G_{12}[GPa]	5.43	S_{12}[MPa]	37.71
v_{12}	0.287	–	–

Figure 6 shows that the SAI specimen is a square plate (150×150 mm). Two overlapping drop-weight coupons are present on the same plate. The dashed rectangles highlight the ROI (region of interest) between the sides and central rails, where the strain fields are measured during the shear test via DIC. Thus, the red rectangle depicts a single coupon for LEI, where the impact hits the center of the dashed rectangle marked by the cross in the ROI—region of interest (Fig. 6). As shown in Fig. 5b, the plate with nine holes (used for 3-rail shear device) is fixed by the clamps of the inertial base of the drop-tower apparatus. After performing the first impact, the plate is rotated and turned upside-down to carry out the second. Thus, two identical impact events are carried out on the same plate but at different positions and faces (top and bottom), as shown in Fig. 1.

experimental fixtures is proposed for SAI analysis based on the standard geometries for impact and shear test as shown in Fig. 6.

Fig. 5 Four toggle clamps and three guiding pins (highlighted by yellow circles) in the base of the drop-tower **a**; SAI specimen fixed in the base by the toggle clamps and constrained by the pins **b**

(a)   (b)
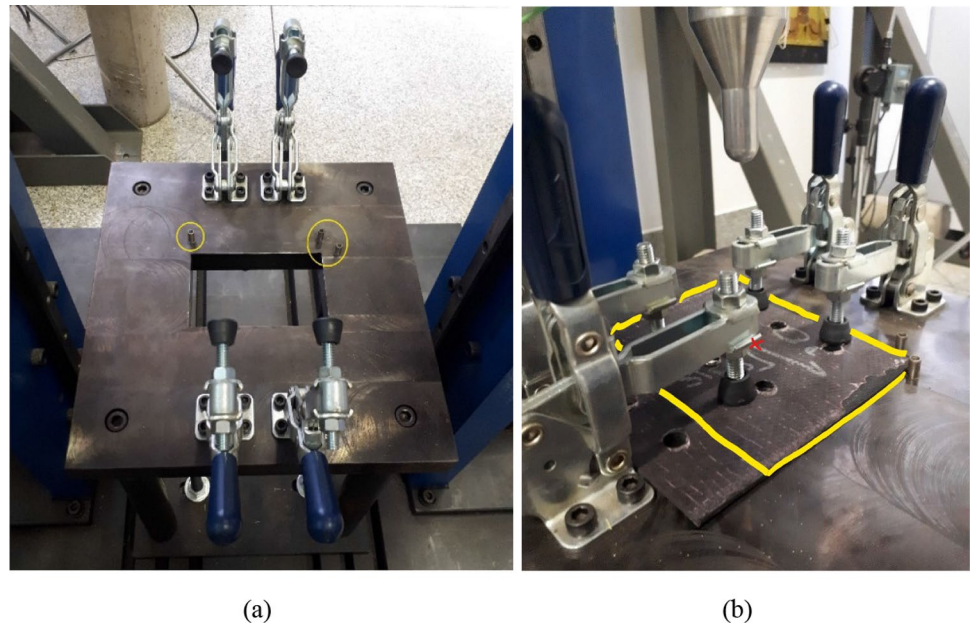
3.2 Experimental tests

In order to observe the intralaminar damage/failure mechanisms and to calculate the damage index, two CFRP plates with $[0°]_{16}$ are manufactured (3.0 mm thick and 95.8 g weight) and tested by using the SAI procedure proposal.

Table 3 shows up the drop-test parameters set up to produce impact damage in the specimens, while Fig. 7 highlights the obtained results for force, displacement, and energy histories and the force–displacement curves of both events (1st and 2nd impact). Moreover, the sample acquisition rate of the DAQ (LabAmp–Kistler™) is set up to 200 kSps and, for a 12 ms impact duration, captures 2400 data points for displacement and forces histories. This high sampling acquisition rate enables us to capture the smallest possible tendencies in these curves and the target's behavior.

In Fig. 7a, high-frequency oscillations are observed in the initial portion of both curves up to approximately 1.0 ms due to the accommodation of the impactor on the target (composite plate). Further oscillations occur due to damage initiation. Damage caused by the second impact is slightly greater than the one caused by the first event, as should be expected. The same behavior is observed in Fig. 7b and c since the maximum displacement are also greater for the second impact. In addition, the second impact duration is higher than the first one due to the necessity of more time to dissipate the transferred kinetic energy. This phenomenon can be noticed as the positive "to-the-right" shift in every analyzed curve that occurs after damage initiation for the second impact (between 1.5 and 2.2 ms). Further oscillations are due to damage evolution through the specimen. Figure 7d shows a permanent indentation whose value must

be considered only an approximation of the true one since the displacement is measured with respect to the drop-tower support and not directly from the specimen (Fig. 3b). The obtained results are summarized in Table 4 for both events.

Based on Fig. 2, the LEI/BVID condition should be evaluated by using the loss-factor theory condition given by Eq. (3). For this case, it is obtained $\zeta_w = 17.7$ with $\lambda = 0.0534$ resulting in the condition $\sqrt{0.68/\lambda} = 3.57$. Therefore, the performed impact can be classified as low-energy $(\zeta_w \geq 3.57)$, and it follows that the condition for a large mass impact (Olsson's target-impactor mass ratio) is satisfied since $M_P = 95.8$ g and $M_i = 4.826$ kg. Moreover, the values presented in Table 4 are considered to be within the BVID limit of 2.0 mm for detailed visual inspection, as heavily discussed in the work developed by Bouvet and Rivallant [11], reassuring that the performed impact tests are low-energy ones.

Then, both pristine and impacted coupons are then subjected to rail tests using the INSTRON universal testing machine and the 3-rail fixture. The shear stress–strain results of both tests are depicted in Fig. 8. It is observed that the behavior of the pristine specimen is in good agreement with the results obtained by the ultimate shear stress for the $[\pm45°]_{4s}$ angle-ply laminate shown in Table 2 (the relative error between both values is around 5.14%).

It can be noticed that there is no significant stiffness reduction between the damaged and pristine coupons due to the impact energy level and the adopted stacking sequence. Since the impact is in a UD (unidirectional) thin laminate, matrix cracks first appear at the non-impacted side of it [5]. The unique noticeable difference between the rail specimens is the premature failure of the damaged one that occurs for
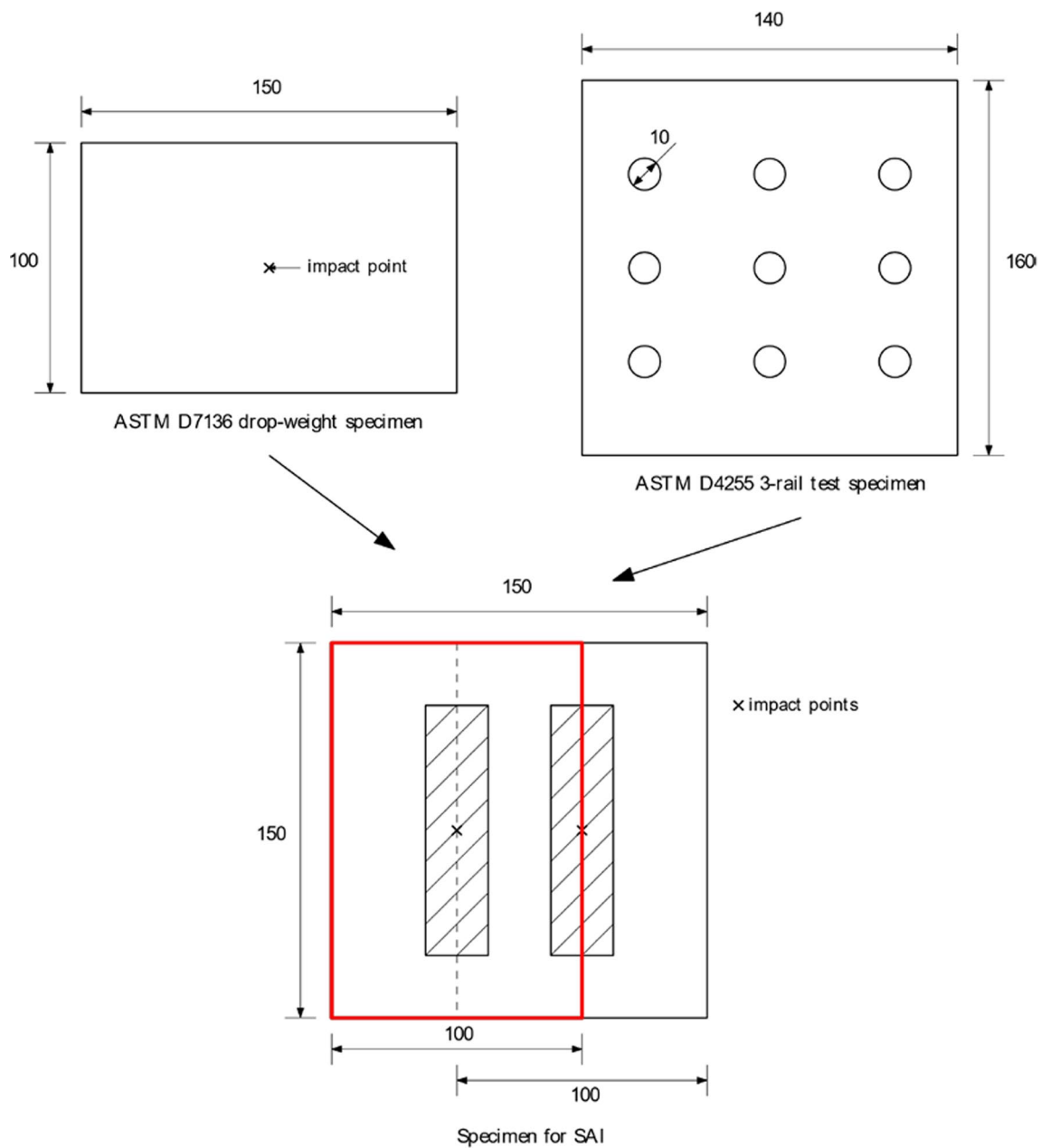
Fig. 6 Coupon geometry proposal for SAI with the red rectangle, which depicts a single coupon for LEI, and the ROI (region of Interest) with hatches

Table 3 Drop-test parameters for the impact events

Impactor mass [kg]	Test height [m]	Initial velocity [m/s]	Impact energy [J]	Impactor radius [mm]
4.826	0.117	1.51	5.53	8.0
Impactor material	Aluminum			
Plate thickness [mm]	3.0			

1.66% shear strain in comparison with the 1.83% of the pristine one at approximately the same stress level (around 33 MPa). Qualitatively, both laminates present the same nonlinear behavior under rail test. Furthermore, both specimens (pristine and impact damaged) are shown in Fig. 9 after the rail tests.
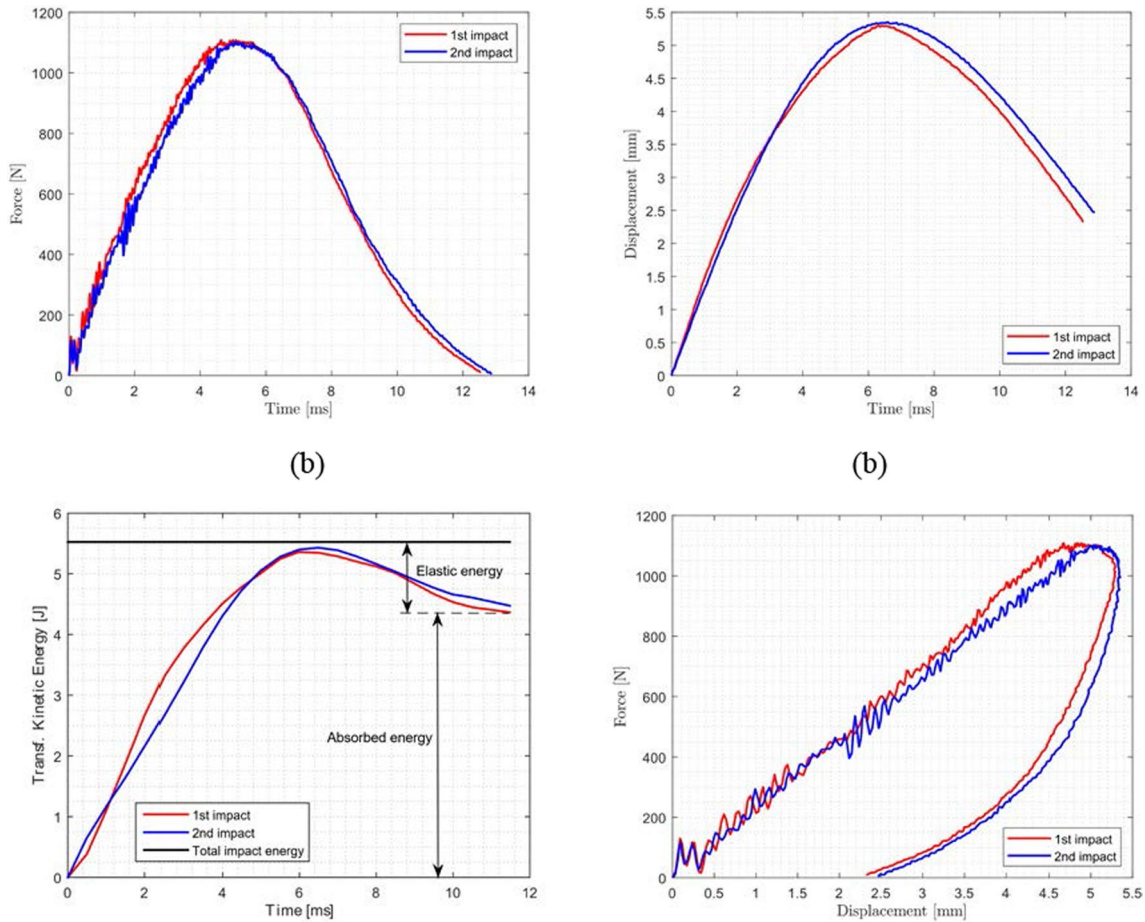
Fig. 7 **a** Impact force history; **b** displacement history; **c** energy history; **d** force–displacement curve for both impact events

Table 4 CFRP drop-tests obtained results summary

Physical quantity	1st impact	2nd impact
Impact duration [ms]	12.54	12.88
Peak force [N]	1108.32	1102.06
Maximum displacement [mm]	5.29	5.35
Permanent indentation [mm]	2.32	2.46
Elastic energy [J]	1.16	1.05
Absorbed energy [J]	4.37	4.48

As can be noticed, in the pristine, the crack onset and propagation occur nearby the moving rail. On the other hand, in the impact-damaged coupon, propagation occurs on the already existing damage with the failure starting at the non-impacted side of the second impact event due to the slightly greater damage initiation, and since the laminate can be considered as a thin one. As expected, damage onset and propagation occur with crack growth at the fibers' direction being parallel to load application, i.e., in the matrix. Besides, it can be noticed in Fig. 10 that the
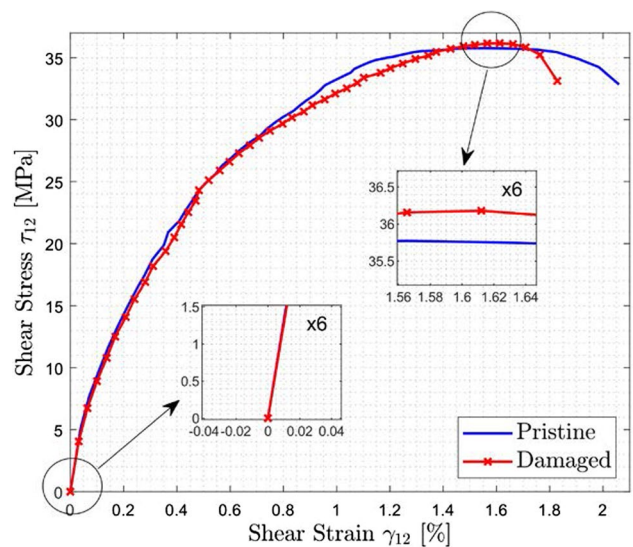

Fig. 8 Shear stress–strain curves: pristine/damaged rail test and angle-ply coupons

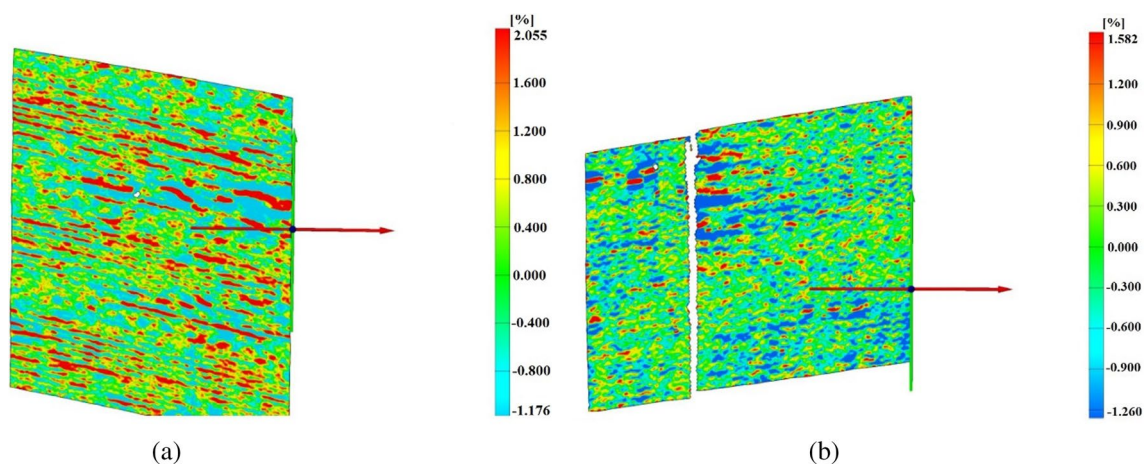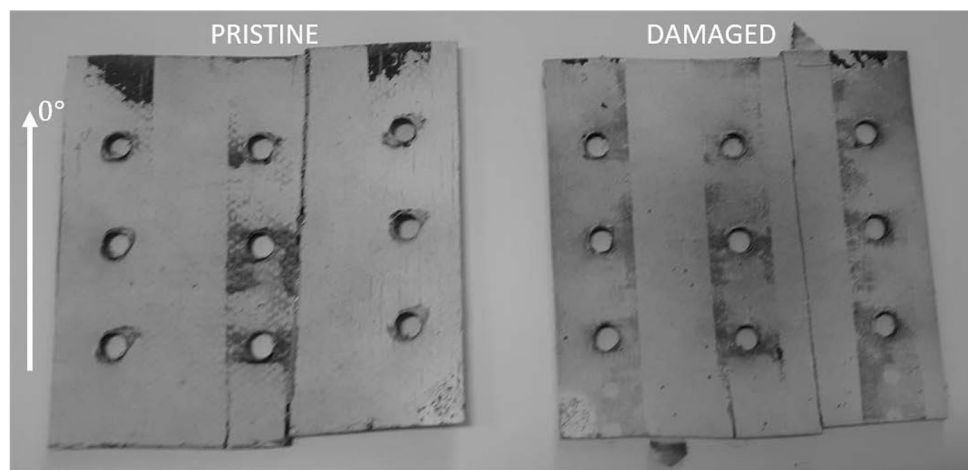**Fig. 9** Pristine and impact-damaged specimens after rail tests

Fig. 10 DIC strain field of **a** pristine coupon; **b** impact-damaged coupon at ultimate shear stresses

obtained strain field by the DIC technique consists of a simple shear stress state in both the pristine and impact-damaged coupons.

Regarding the damage index, it is expected a low value due to the similarity between the stress–strain curves. For this particular case study, the minimum allowable energy is equal to $E_D^{\min} = 0.0723$ J/mm³, while $E_P = 0.4769$ J/mm³ and $E_D = 0.3889$ J/mm³ providing a $\mathrm{DI_{SAI}} = 0.2175$ indicating that the LEI induced damage in the sample, but not a much severe one.

Considering a composite structure design with a focus on impact requirements, SAI damage index should be determined for other impact energy levels, which would cause different damage levels in the laminate. Therefore, in the next section, through computational simulations, different DI values are going to be obtained assuming different impact damage levels. To do this type of evaluation, a User Material Subroutine (UMAT) linked to ABAQUS will be implemented to simulate the rail tests of impact-damaged composite coupons.

4 Computational simulations

Based on the computational simulations, it is possible to analyze the post-impact behavior of composite laminates using a material model that accounts for progressive failure. Therefore, in this section, a material model based on the continuum damage mechanics, which was implemented as a user material subroutine (UMAT), is shown and discussed. It is important to highlight that several previous works developed by the present authors and others were conducted to investigate aspects related to finite element mesh convergences, as well as model parameters identification and a better understanding of the model limitations and capabilities [14, 15, 38, 41–43].

4.1 Material model

Due to the inherent anisotropy and heterogeneous nature of composite materials, modeling their failure modes is a complex task. In this context, for models that account for progressive failure, damage evolution is not modeled with ease since intralaminar mechanisms interact between them and from these can trigger interlaminar failure. For engineering purposes, it is interesting that a material model, which is a mandatory requirement for the simulation using commercial FEA software [29], has three main characteristics, that are: (a) to require simple tests for the identification of its parameters, (b) to be easy for coupon manufacturing for mechanical characterization, and (c) that it can be easily implemented as a routine with low computational cost [30–35].

Continuum damage mechanics is the study, through mechanical variables, of the deterioration that a material presents when subjected to some loading and its evolution through damage accumulation. Within its framework, it is a thermodynamic consistent failure theory, following the Clausius–Duhem inequality so that the second law is satisfied, i.e., damage is an irreversible process. Besides, CDM deals with quantities (e.g., stress, strain, temperature, internal variables) based on the assumption of continuity, which means that these represent average values over a representative volume element (RVE) that in its turn allows a non-local description of the material state in a given point "P" using homogenization procedures [36]. In addition, the size of the RVE represents the mesoscale, while voids and cracks are at the microscale [37]. Therefore, CDM-based material models are capable of satisfying the aforementioned (a), (b), and (c) aspects with fidelity regarding the physical phenomena. In other words, a phenomenological mesoscale 2D material model based on CDM can be written as a UMAT linked to ABAQUS finite element package. In the present work, the material model proposal is based on the criteria developed by Ferreira et al. [38], Ribeiro [30], and Ladevèze's model [39]. Thus, the proposed model is formulated to simulate composite materials with unidirectional (UD) reinforcement, where lamina homogenization is done to capture tensile and compression failures in direction 1 (aligned to the fibers) and 2 (normal to the fibers) and failure due to in-plane shear without being capable to account for the fiber-matrix interface behavior. It is an intralaminar material model, which does not account for delamination. Moreover, the onset of failure mechanisms is made separately since the fiber and matrix elasticity moduli show different orders of magnitude. However, the evolution of degradation considers the interaction between the damage modes, which is shown by the modified constitutive matrix, as proposed by Matzenmiller [40] and given in Eq. (9).

$$D = \frac{1}{K} \begin{bmatrix} (1-d_1)E_{11} & (1-d_1)(1-d_2)\nu_{21}E_{22} & 0 \\ (1-d_1)(1-d_2)\nu_{11}E_{11} & (1-d_2)E_{22} & 0 \\ 0 & 0 & K(1-d_6)G_{12} \end{bmatrix}$$
(9)

where $K = 1 - (1-d_1)(1-d_2)\nu_{12}\nu_{21}$ in which d_i are the damage internal variables, and $\nu_{ij}(i, j = 1, 2 \forall i \neq j)$ are the Poisson's ratios. So, the linear elastic constitutive equation for the damaged material is written according to the principle of strain equivalence that states, in the words of Lemaitre [36]: "*any strain constitutive equation for a damaged material may be derived in the same way as for a virgin material except that the usual stress is replaced by the effective stress.*" Therefore, denoting $\hat{\sigma}$ and ϵ as the effective stresses and equivalent strains, respectively, it follows that $\hat{\sigma} = D\epsilon$.

4.1.1 Ply behavior in direction 1

Under tensile loading, the behavior of the ply in direction 1 is considered to follow a linear elastic behavior presenting a brittle failure with independency of fiber volume fraction and lamina Young's moduli. The maximum stress criterion is then used and is given by Eq. (10) as,

$$\frac{\sigma_{11}}{X_T} \geq 1$$
(10)

in which X_T is the longitudinal tensile strength. For the finite element analysis, the value of its associated damage variable d_1 is assumed as 0.99 once failure is detected, considering that the reinforcement is fully damaged. In theory, this should be in the interval $d_1 \in [0, 1]$ assuming a null value for undamaged and 1 for fully damaged. However, this is done to avoid issues with localization during the simulations. Also, the degradation of properties is done at the end of each time step of the finite element solution instead of during each iteration procedure. This is verified and performed in many works published by other authors [30, 31, 38, 41–43].

The compressive behavior of the ply in direction 1 assumes a linear elastic stress–strain behavior until it reaches a threshold value. The linear elastic limit is experimentally identified via compression tests on 0° coupons, which is denoted as X_{C_0} and is found by the intersection value of the parallel curve with 0.2% strain with the experimental curve. In the linear elastic regime, the criterion is given by Eq. (11).

$$\frac{|\sigma_{11}|}{X_{C_0}} \geq 1$$
(11)

Thus, after the compressive stress reaches X_{C_0}, any increasing in load results in a nonlinear behavior, which is modeled by the secant modulus strategy, given as:

$$E_{11} = \frac{X_{C_0}}{|\varepsilon_{11}|}\left[1 - f(\varepsilon_{11})\right] + f(\varepsilon_{11})E_{11_0} \tag{12}$$

in which E_{11_0} is the initial Young's modulus in the longitudinal direction, $f(\varepsilon_{11})$ is the strain function obtained from the linear equation that best fits the experimental data of the stress curve, ε_{11} is the strain at the fiber direction and E_{11} is the secant modulus. Thus, damage is detected by the effect of loss of stiffness in the nonlinear region, i.e., by the decay on the slope in each successive iteration.

4.1.2 Ply behavior in direction 2 and due to in-plane shear

Many works support that the behavior of the ply in direction 2 is nonlinear under compression. Besides, the in-plane stress state damage process is driven by transverse stress and in-plane shear [27, 28, 41, 44]. The present work also assumes that stresses in direction 1 do not affect the damage state in direction 2 and due to in-plane shear. Thus, based on Ribeiro's [30, 31] and Ferreira's [38] approaches, it is proposed a damage threshold limit based on the experimental tensile and compression test data of angle-ply and off-axis coupons, which are given as,

$$f_+ = 1 - \left(\frac{-0.018\sigma_{22}^2 - 0.474\sigma_{22} + S_{12}}{|\tau_{12}|}\right), \quad \sigma_{22} \geq 0 \tag{13a}$$

$$f_- = 1 - \left(\frac{-0.004\sigma_{22}^2 + 0.363\sigma_{22} + S_{12}}{|\tau_{12}|}\right), \quad \sigma_{22} < 0 \tag{13b}$$

in which S_{12} is the in-plane shear strength, τ_{12} is the shear stress, σ_{22} is the transverse stress and that, for both cases of

Eq. (13), it follows that $f_{+,-} = 0$ represents the threshold limit for damage initiation. Furthermore, the f_- portion of the $\sigma_{22}x\tau_{12}$ envelope (Fig. 11) is obtained from experimental data gathered by Ribeiro [30], while the f_+ portion uses data from tensile tests on $[70°]_6$ and $[45°]_6$ off-axis coupons, as well as from $[\pm45°]_{4s}$ angle-ply and $[90°]_8$ UD coupons, as shown in Fig. 11.

Furthermore, under compression the nonlinear behavior starts after a linear threshold value Y_{C_0} that is obtained analogously to X_{C_0}, and progresses obeying a secant strategy as well. Thus, it follows,

$$E_{22} = \frac{Y_{C_0}}{|\varepsilon_{22}|}\left[1 - g(\varepsilon_{22})\right] + g(\varepsilon_{22})E_{22_0} \tag{14}$$

where E_{22_0} is the initial Young's modulus in the transverse direction (normal to the fibers) and $g(\varepsilon_{22})$ is the strain function obtained from parameter fitting of 90° coupons under compression. In order to model damage evolution in the matrix, the damage variables d_2 and d_6, respectively, associated with σ_{22} and τ_{12} are used. In CDM, the effective stress hypothesis relates these damage variables to the lamina stress state [45] and, considering that those are applied on the damaged area, it follows:

$$\begin{Bmatrix} \hat{\sigma}_{11} \\ \hat{\sigma}_{22} \\ \hat{\tau}_{12} \end{Bmatrix} = \begin{bmatrix} \frac{1}{1-d_1} & 0 & 0 \\ 0 & \frac{1}{1-d_2} & 0 \\ 0 & 0 & \frac{1}{1-d_6} \end{bmatrix} \begin{Bmatrix} \sigma_{11} \\ \sigma_{22} \\ \tau_{12} \end{Bmatrix} \tag{15}$$

Notice that Eq. (15) is written in the material coordinate system. Provided with effective stresses (quantities with a "hat"), the strain energy density for the damaged polymeric matrix E_D is

$$E_D = \frac{1}{2}\left[\frac{\langle\sigma_{22}\rangle_+^2}{E_{22_0}(1-d_2)} + \frac{\langle\sigma_{22}\rangle_-^2}{E_{22_0}} + \frac{|\tau_{12}|^2}{G_{12_0}(1-d_6)}\right] \tag{16}$$
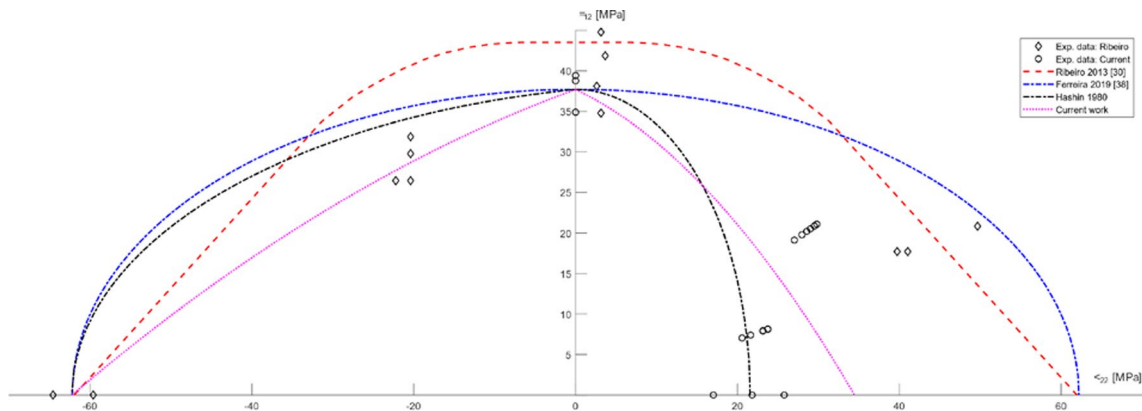

Fig. 11 $\sigma_{22}x\tau_{12}$ envelope and threshold limits

in which $\langle x \rangle_{+,-}$ is the Macaulay brackets operator and G_{12_0} is the initial in-plane shear modulus. Furthermore, Eq. (16) can be related to the thermodynamic forces Y_2 and Y_6, using its associated damage variables, for the ply [39].

$$Y_2 = \frac{\partial E_D}{\partial d_2} = \frac{\langle \sigma_{22} \rangle_+^2}{2E_{22_0}(1 - d_2)^2} \tag{17a}$$

$$Y_6 = \frac{\partial E_D}{\partial d_6} = \frac{\tau_{12}^2}{2G_{12_0}(1 - d_6)^2} \tag{17b}$$

In Eq. (17), it is considered that under transverse tension, d_2 only grows for $\sigma_{22} \geq 0$ and d_6 grows independently of the sign of τ_{12}. There is also the coupled case of transverse tension and in-plane shear that influences the damage process. This mutual influence varies from material to material and, in the present model, it is simply a linear combination of the associated thermodynamic forces as stated by Ladevèze [39]:

$$\hat{Y} = Y_6 + bY_2 \tag{18}$$

where b is the coupling coefficient and $\hat{Y}$ is the thermodynamic force related to the combined state.

Furthermore, quasi-static cyclic tensile tests in $[\pm45°]_{4s}$, $[90°]_8$, $[70°]_6$ and $[45°]_6$ coupons were conducted to obtain the necessary parameters to model damage evolution under transverse tension, in-plane shear and in the coupled cases to feed the numerical model during simulations as shown in the literature [46]. Table 5 compiles the identified material model parameters used.

The evolution laws are obtained by experimental fit and are depicted as $d_2 = 0.036\sqrt{Y_2} - 0.048$ and $d_6 = 0.045\sqrt{Y_6} - 0.099$.

4.2 Damage index predicted by computational simulations

Finite element simulations are carried out aiming to obtain a computationally predicted damage index, also investigating some of the tendencies that should be observed experimentally. Some study cases are selected, arbitrarily degrading

Table 5 Material model parameters

Parameter	Value/Law	Unit
X_{C_0}	253	MPa
Y_{C_0}	60.3	MPa
b	1.459	–
$f(\varepsilon_{11})$	$78.873\varepsilon_{11} + 1.087$	–
$g(\varepsilon_{22})$	$4.176\varepsilon_{22} + 0.032$	–

mechanical properties, such as E_{22}, G_{12}, and v_{12} by a percentage value of the pristine one in the impact-damaged region. The estimation of this region is done by a visual inspection with the aid of a magnifier and following the semi-analytical approach proposed by Abrate [5]. Degradation percentages are assumed to be equal to 5%, 10%, 15%, 20%, 30%, and 50% of the original values of mechanical properties. The FE model has a simple rectangular geometry, which is equal to the ROI (region of interest), with 27.5-mm width and 150-mm length meshed by S8R quadrilateral shell elements with eight nodes, six DoF/node, and reduced integration. The mesh density was defined after a convergence analysis to be described. Boundary conditions are given by encastre at the fixed side and a prescribed displacement of 2.0 mm in the x-direction at the free rail side as shown in Fig. 12.

The impact-damaged region is modeled as a partition of the model accounting for the degraded properties as depicted in Fig. 12. It is also modeled as a rectangle, and not as an ellipse, since it is easier to mesh the model, and, mainly, because the observed trends should not be very different adopting one or another, considering [0°] as stacking sequence. Besides, the size of the damaged region (20 mm × 8 mm) is fixed for all study cases to avoid adding another parameter to be considered during the analyses.
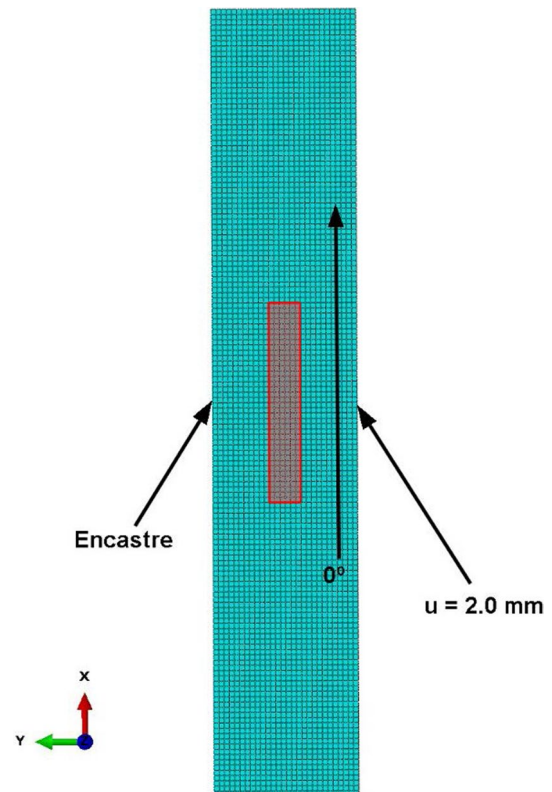

Fig. 12 FE model of the rail test specimen highlighting the impact-damaged region (in red)

The estimation of the damaged region inside the ROI (region of interest) follows a semi-analytical approach based on Abrate's work [5]. Accordingly, this LEI-damaged region has an elliptical shape in which the ellipse radii a and b are given as,

$$a = 2\sqrt{\pi}\left(\frac{D_{11}}{m}\right)^{\frac{1}{4}}[2(A+1)]^{\frac{1}{8}}\sqrt{t}, \tag{19a}$$

$$b = \frac{a}{\left(D_{11}/D_{22}\right)^{1/4}} \tag{19b}$$

where D_{ij} are the components of the bending-torsion stiffness matrix from CLT (classical laminate theory), m is the specimen mass, and t is the impact duration time that can be estimated or experimentally obtained. It is important to highlight that in the present study, the second one was adopted. The parameter A is the stiffness ratio and is given by,

$$A = \frac{D_{12} + 2D_{66}}{\sqrt{D_{11}D_{22}}} \tag{20}$$

The radii values obtained for the tested coupon are $a = 20$ mm and $b = 8$ mm, which are approximately near the real ones. A simple visual inspection with the aid of a magnifier and the classical established tap testing (i.e., usage of sound cues as a non-destructive test) was also performed, aiming to estimate the impact-damaged region. Obtained values are $a \approx 16$ mm and $b \approx 6$ mm, with those being similar to the ones obtained using Abrate's approach. Thus, being conservative, the authors arbitrarily decided to use the biggest ones. Notice that these values describe an impact-damaged region confined in the ROI during shear-after-impact testing.
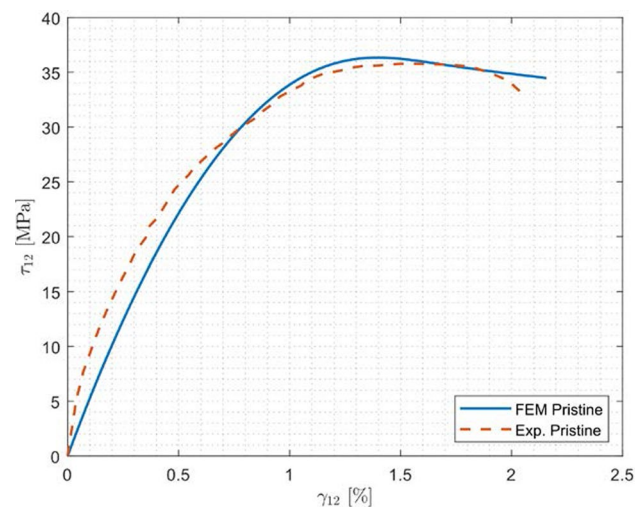
The first step of computational simulations consists of evaluating the model for the pristine case, comparing the numerical prediction with experimental stress–strain results as shown in Fig. 13. As can be noticed, the experimental and computational analysis present similar tendencies with some discrepancies in the initial portion of the curves. Besides, no significant differences are observed with values of ultimate/fracture shear stresses and strains being very close to each other.

Following up on the degradation study cases, the obtained results in terms of shear stress–strain curves for the pristine and damaged FE models are depicted in Fig. 14. Again, mesh convergence is considered for maximum relative errors of 5% between the variables of interest from one mesh result to another.

It can be noticed that for higher degradation, i.e., greater impact damage (or impact energy), the ultimate and fracture shear strains and stresses are lower, representing a premature failure of the specimen as damage increases. Besides, a decrease in stiffness is not observed between the curves for the pristine and 5–20% of degradation. On the other hand, the results for 30% of degradation present a slight variation in stiffness, while this can be well-noticed for the curve of 50% degradation. Moreover, as degradation increases, it is expected that the SAI damage index also grows, as can be checked in Table 6 and Fig. 15.

In Fig. 15, it can be verified that the values of DI_{SAI} were obtained by comparing the energy densities from each simulation with the FE result for the pristine laminate. Based on the numerical results, a quadratic curve fitting is performed to have an approximation of the degradation level present in the experimental impact-damaged coupon. Considering it, the analysis approach employed and simplifications adopted
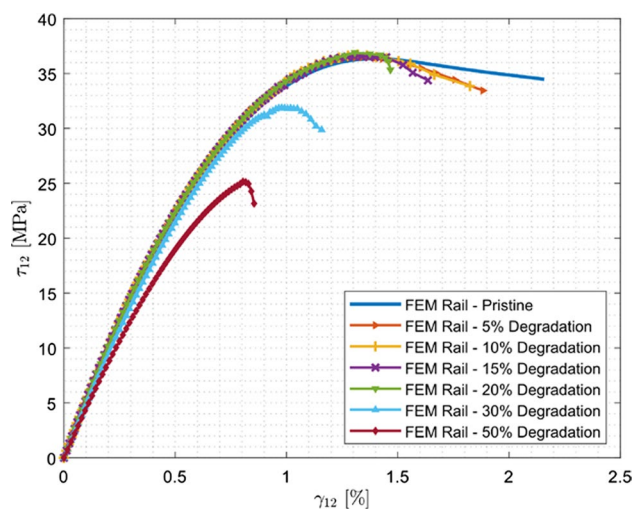

Fig. 13 Shear stress–strain curves for the pristine coupon: computational vs. experimental results

Fig. 14 Computational shear stress–strain curves of rail tests: pristine and damaged coupons with different levels of degradation that could be caused by impact events

Table 6 Shear-after-impact damage index predicted via computational analyses

Level of degradation	5%	10%	15%	20%	30%	50%
Damage index value	0.2267	0.2741	0.4321	0.5714	0.8798	1.0
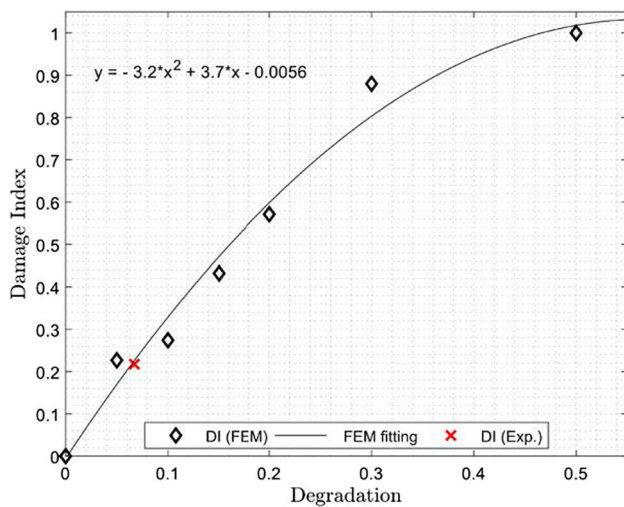
Fig. 15 Computationally obtained curve for the damage index as a function of the degradation level

for the computational model, it could be said that the experimental drop-weight test induced damage that degraded the material elastic properties closely to 5% (the exact value is 6.7%) of its original values with relation to the undamaged ones (since $DI_{SAI}^{exp} = 0.2175$). However, this can only be considered as an approximation since, in reality, the damaged region and mechanical properties change in terms of different impact energy levels.

5 Conclusions

The impact (low-energy) and post-impact behavior of CFRP plates under in-plane (simple) shear with UD (unidirectional) stacking sequence under the BVID limit were experimentally investigated. For this, it is proposed a procedure for the shear-after-impact analysis, which includes 3-rail and drop-weight testing devices. The shear-after-impact experimental analysis approach is proposed based on the comparison of shear stress–strain behavior of pristine and impact-damaged specimens. To fit both fixtures, a new coupon is designed and tested under the proposed guidelines with the obtained results, showing that the procedure is promising for being used as a tool for residual strength assessment of laminated composite materials. Further experiments and studies are recommended for significant statistical data gathering but, as an overall, both tested coupons showed up the expected trends.

Regarding damage quantification, a new index was proposed. Since for composite materials it is difficult to define one metric that incorporates all variables relevant to the problem, the damage index for SAI followed up a phenomenological strategy defined by energy density ratio values. These are gathered from the shear stress–strain curves obtained from 3-rail tests and make the damage index calculation simple. Therefore, firstly, submit a pristine coupon under 3-rail testing to obtain its shear stress–strain curve and integrate it. From the ultimate value of shear stress, a minimum allowable energy density is obtained. Then, drop-weight tests are carried out to introduce damage in another coupon, and a posterior 3-rail shear test is conducted in it to obtain the stress–strain curve. Consequently, the energy density for the damaged laminate is obtained, and if it is between the range $E_D^{min} \leq E_D \leq E_P$, then the damage index DI_{SAI} is calculated using Eq. (7) and, with it, the severity of damage is easily assessed.

Furthermore, some computational simulations were successfully made to obtain different values of damage indexes for different impact levels (i.e., different impact damage). Using a material model, which was written as a UMAT linked to ABAQUS, it was possible to obtain the damage index from computational analysis. Thus, it was verified the expected tendency of obtaining higher DI_{SAI} values for higher degradation values (i.e., impact energy values). It is known that is necessary to include an impact model in the computational analysis in order to have quantitative relevant results, but that fits in future works proposals since the main goal of the present work was of proposing a SAI analysis procedure, and a damage index for the damage severity quantification. In this sense, SAI tests can be considered as a complementary analysis for the compression-after-impact and flexure-after-impact tests with the ideal case being the one in which the post-impact structural integrity is evaluated by combining results from all three analyses for a more holistic damage tolerance design.

References

1. Beaumont PWR, Soutis C, Hodzic A (eds) (2017) The structural integrity of carbon fiber composites: fifty years of progress and achievement of the science, development, and applications. Springer International Publishing, Switzerland

2. Jones RM (1998) Mechanics of composite materials. CRC Press, London

3. Hinton M, Kaddour AS, Soden PD (2004) Failure criteria in fibre reinforced polymer composites: the world-wide failure exercise. Elsevier, London. https://doi.org/10.1016/B978-0-080-44475-8.X5000-8

4. Kaddour AS, Hinton M (2013) Maturity of 3D failure criteria for fibre-reinforced composites: comparison between theories and experiments: Part B of WWFE-II. J Compos Mater 47(6–7):925–966. https://doi.org/10.1177/0021998313478710

5. Abrate S (1998) Impact on composite structures. Cambridge University Press, Cambridge

6. De Oliveira SAC, Donadon MV, Arbelo MA (2020) Crushing simulation using an energy-based damage model. J Braz Soc Mech Sci Eng 42:1–16. https://doi.org/10.1007/s40430-020-02383-6

7. Özbek Ö, Dogan NF, Bozkurt ÖY (2020) An experimental investigation on lateral crushing response of glass/carbon intraply hybrid filament wound composite pipes. J Braz Soc Mech Sci Eng 42(7):1–13. https://doi.org/10.1007/s40430-020-02475-3

8. Feli S, Jafari SS (2017) Analytical modeling for perforation of foam-composite sandwich panels under high-velocity impact. J Braz Soc Mech Sci Eng 39(2):401–412. https://doi.org/10.1007/s40430-016-0489-7

9. Thorsson SI, Waas AM, Rassaian M (2018) Low-velocity impact predictions of composite laminates using a continuum shell based modeling approach Part a: impact study. Int J Solids Struct 155:185–200. https://doi.org/10.1016/j.ijsolstr.2018.07.020

10. Thorsson SI, Waas AM, Rassaian M (2018) Low-velocity impact predictions of composite laminates using a continuum shell based modeling approach Part B: BVID impact and compression after impact. Int J Solids Struct 155:201–212. https://doi.org/10.1016/j.ijsolstr.2018.07.018

11. Bouvet C, Rivallant S (2016) Damage tolerance of composite structures under low-velocity impact. Dynamic deformation, damage and fracture in composite materials and structures. Woodhead Publishing, Darya Ganj. https://doi.org/10.1016/B978-0-08-100080-9.00002-6

12. Travessa AT (2006) Simulation of delamination in composites under quasi-static and fatigue loading using cohesive zone models. Ph.D. Thesis, University of Girona

13. Gliszczynski A, Kubiak T, Rozylo P, Jakubczak P, Bienias J (2019) The response of laminated composite plates and profiles under low-velocity impact load. Compos Struct 207:1–12

14. De Medeiros R (2016) Development of a criterion for predicting residual strength of composite structures damaged by impact loading. Ph.D. Thesis, University of São Paulo

15. De Medeiros R, Vandepitte D, Tita V (2018) Structural health monitoring for impact damaged composite: a new methodology based on a combination of techniques. Struct Health Monit 17(2):185–200. https://doi.org/10.1177/1475921716688442

16. Feng Y, He Y, Tan X, An T, Zheng J (2017) Investigation on impact damage evolution under fatigue load and shear-after-impact-fatigue (SAIF) behaviors of stiffened composite panels. Int J Fatigue 100:308–321. https://doi.org/10.1016/j.ijfatigue.2017.03.046

17. Feng Y, He Y, Tan X, An T, Zheng J (2017) Experimental investigation on different positional impact damages and shear-after-impact (SAI) behaviors of stiffened composite panels. Compos Struct 178:232–245. https://doi.org/10.1016/j.compstruct.2017.06.053

18. American Society for Testing and Materials—D7136 (2015) Standard test method for measuring the damage resistance of a fiber-reinforced polymer matrix composite to a drop-weight impact event. ASTM International, West Conshohocken. https://doi.org/10.1520/D7136_D7136M-20

19. American Society for Testing and Materials—D4255 (2015) Standard test method for in-plane shear properties of polymer matrix composite materials by the rail shear method. ASTM International, West Conshohocken. https://doi.org/10.1520/D4255_D4255M-20

20. Christoforou AP, Yigit AS (1998) Characterization of impact in composite plates. Compos Struct 43(1):15–24. https://doi.org/10.1016/S0263-8223(98)00087-7

21. Christoforou AP (2001) Impact dynamics and damage in composite structures. Compos Struct 52(2):181–188. https://doi.org/10.1016/S0263-8223(00)00166-5

22. Christoforou AP, Elsharkawy AA, Guedouar LH (2001) An inverse solution for low-velocity impact in composite plates. Comput Struct 79(29–30):2607–2619. https://doi.org/10.1016/S0045-7949(01)00113-4

23. Yigit AS, Christoforou AP (2007) Limits of asymptotic solutions in low-velocity impact of composite plates. Compos Struct 81(4):568–574. https://doi.org/10.1016/j.compstruct.2006.10.006

24. Christoforou AP, Yigit AS (2009) Scaling of low-velocity impact response in composite structures. Compos Struct 91(3):358–365. https://doi.org/10.1016/j.compstruct.2009.06.002

25. Olsson R (1992) Impact response of orthotropic composite plates predicted from a one-parameter differential equation. AIAA J 30(6):1587–1596. https://doi.org/10.2514/3.11105

26. American Society for Testing and Materials—D3529 (2016) Standard test method for constituent content of composite prepreg. ASTM International, West Conshohocken. https://doi.org/10.1520/D3529-16

27. American Society for Testing and Materials – D3039 (2017) Standard test method for tensile properties of polymer matrix composite materials. ASTM International, West Conshohocken. https://doi.org/10.1520/D3039_D3039M-17

28. American Society for Testing and Materials—D3518 (2013) Standard test method for in-plane shear response of polymer matrix composite materials by tensile test of a 45° laminate. ASTM International, West Conshohocken. https://doi.org/10.1520/D3518_D3518M-18

29. Majzoobi GH, Jafari SS (2021) An investigation into the effect of strain rate on damage evolution in pure copper using a modified Bonora model. J Stress Anal 6(1):127–138. https://doi.org/10.22084/jrstan.2021.24907.1193

30. Ribeiro ML, Tita V, Vandepitte D (2012) A new damage model for composite laminates. Compos Struct 94(2):635–642. https://doi.org/10.1016/j.compstruct.2011.08.031

31. Ribeiro ML, Vandepitte D, Tita V (2013) Damage model and progressive failure analysis for filament wound composite laminates. Appl Compos Mater 20:975–992. https://doi.org/10.1007/s10443-013-9315-x

32. Tita V, de Carvalho J, Vandepitte D (2008) Failure analysis of low velocity impact on thin composite laminates: experimental and

numerical approaches. Compos Struct 83(4):413–428. https://doi.org/10.1016/j.compstruct.2007.06.003

33. Pinho ST, Davila CG, Camanho PP, Iannucci L, Robinson P (2005) Failure models and criteria for FRP under in-plane or three-dimensional stress states including shear non-linearity. NASA Technical Reports, NASA/TM-2005–213530

34. Davila CG, Camanho PP, Rose CA (2005) Failure criteria for FRP laminates. Compos Mater 39(4):323–345. https://doi.org/10.1177/0021998305046452

35. Donadon MV, Iannucci L, Falzon BG, Hodgikinson JM, de Almeida SFM (2008) A progressive failure model for composite laminates subjected to low velocity impact damage. Compos Struct 86(11–12):1232–1252. https://doi.org/10.1016/j.compstruc.2007.11.004

36. Lemaitre J (2012) A course on damage mechanics. Springer Science & Business Media, Cham

37. Talreja R (2008) Damage and fatigue in composites—a personal account. Compos Sci Technol 68(13):2585–2591. https://doi.org/10.1016/j.compscitech.2008.04.042

38. Ferreira GFO, Ribeiro ML, Ferreira AJM, Tita V (2019) Computational analyses of composite plates under low-velocity impact loading. Mater Today: Proc 8:778–788. https://doi.org/10.1016/j.matpr.2019.02.020

39. Ladeveze P, LeDantec E (1992) Damage modelling of the elementary ply for laminated composites. Compos Sci Technol 43(3):257–267. https://doi.org/10.1016/0266-3538(92)90097-M

40. Matzenmiller A, Lubliner J, Taylor RL (1995) A constitutive model for anisotropic damage in fiber-composites. Mech Mater 20(2):125–152. https://doi.org/10.1016/B978-008044475-8/50028-7

41. Almeida JHS Jr, Tonatto MLP, Ribeiro ML, Tita V, Amico SC (2018) Buckling and post-buckling of filament wound composite tubes under axial compression: linear, nonlinear, damage and experimental analyses. Compos B Eng 149:227–239. https://doi.org/10.1016/j.compositesb.2018.05.004

42. Almeida JHS Jr, Ribeiro ML, Tita V, Amico SC (2017) Stacking sequence optimization in composite tubes under internal pressure based on genetic algorithm accounting for progressive damage. Compos Struct 178:20–26. https://doi.org/10.1016/j.compstruct.2017.07.054

43. Jr Almeida JHS, Ribeiro ML, Tita V, Amico SC (2016) Damage and failure in carbon/epoxy filament wound composite tubes under external pressure: experimental and numerical approaches. Mater Des 96:431–438. https://doi.org/10.1016/j.matdes.2016.02.054

44. Puck A, Schürmann H (2004) Failure analysis of FRP laminates by means of physically based phenomenological models. Failure criteria in fibre-reinforced-polymer composites. Elsevier, London, pp 832–876. https://doi.org/10.1016/j.jmrt.2014.10.003

45. Herakovich CT (1998) Mechanics of fibrous composites. John Wiley & Sons, New York

46. Souza GSC (2021) Evaluation of laminated composite plates behavior under shear-after-impact loading conditions: a methodology proposal. MSc Dissertation. University of São Paulo